

Anion vacancies activate N₂ to ammonia on Ba–Si orthosilicate oxynitride-hydride

Received: 15 February 2024

Accepted: 13 January 2025

Published online: 17 February 2025



Zhujun Zhang^{1,4,5}, Kazuki Miyashita^{1,5}, Tong Wu¹, Jun Kujirai¹, Kiya Ogasawara¹, Jiang Li¹, Yihao Jiang¹, Masayoshi Miyazaki¹, Satoru Matsuishi^{1,2}, Masato Sasase¹, Tomofumi Tada¹✉, Hideo Hosono^{1,2}✉ & Masaaki Kitano^{1,3}✉

Anion vacancies on metal oxide surfaces have been studied as either active sites or promoting sites in various chemical reactions involving oxidation/reduction processes. However, oxide materials rarely work effectively as catalysts in the absence of transition metal sites. Here we report a Ba–Si orthosilicate oxynitride–hydride as a transition-metal-free catalyst for efficient ammonia synthesis via an anion-vacancy-mediated mechanism. The facile desorption of H[−] and N^{3−} anions plus the flexibility of the crystal structure can accommodate a high density of electrons at vacancy sites, where N₂ can be captured and directly activated to ammonia through hydrogenation processes. The ammonia synthesis rates reach 40.1 mmol g^{−1} h^{−1} at 300 °C by loading ruthenium nanoparticles. Although not found to dissociate N₂, Ru instead facilitates the formation of anion vacancies at the Ru–support interface. This demonstrates a new route for anion-vacancy-mediated heterogeneous catalysis.

Oxygen vacancies on oxide-based catalysts sometimes play a key role in various chemical reactions. For example, the oxidation of organic molecules effectively proceeds over a V₂O₅ catalyst, in which the lattice oxygen of V₂O₅ reacts with the substrate to form V₂O_{5−x} (x, oxygen vacancy) and is regenerated by gas-phase O₂ molecules¹. The redox between V⁵⁺ and V⁴⁺ is the driving force for this reaction, which is well known as the Mars–van Krevelen mechanism. In oxide-supported metal catalysts, oxygen vacancy sites directly activate the reactant molecule (Mars–van Krevelen mechanism) or indirectly promote the supported metal sites through electronic metal–support interaction^{2,3}. In any case, transition metal (TM) sites, including lattice metal cations and/or the supported metal, are essential to activate various molecules in catalysis. In other words, oxide materials do not work effectively as catalysts in the absence of TM sites.

Ammonia synthesis also occurs on the surface of TMs such as Fe and Ru (refs. 4,5). The overall reaction rate is governed by the

nitrogen binding energy (E_N) of the TM because the N₂ dissociation is the rate-determining step (RDS). This leads to the establishment of a volcano-shaped relationship between the ammonia synthesis activity and E_N (refs. 6,7). Most studies in the past two decades have been focused on the development of efficient oxide-based supports or promoters that would enhance electron transfer to the TM sites and thus facilitate N≡N bond weakening through metal-to-N₂ π backdonation^{8,9}. Electride and hydride-based catalysts were recently demonstrated to exhibit enhanced activity for ammonia synthesis under mild reaction conditions^{10–15}. In addition, the N₂ reduction to NH₃ is facilitated by the redox properties of the lattice TM sites, such as Ce in BaCeO_{1.80}H_{0.57}N_{0.23} (ref. 16) and Ti in BaTiO_{2.5}H_{0.5} (ref. 17). However, although these new strategies promote ammonia synthesis efficiency, TMs are still irreplaceable as active centres for N₂ dissociation in most cases. Only alkali or alkali earth metal hydrides such as KH and BaH₂ have been reported to function as catalysts for ammonia synthesis in the absence of TMs

¹MDX Research Center for Element Strategy, Institute of Integrated Research, Institute of Science Tokyo, Yokohama, Japan. ²MANA Center,

National Institute for Materials Science, Tsukuba, Japan. ³Advanced Institute for Materials Research (WPI-AIMR), Tohoku University, Sendai, Japan.

⁴Present address: State Key Laboratory of Materials-Oriented Chemical Engineering, College of Chemical Engineering, Nanjing Tech University, Nanjing, People's Republic of China. ⁵These authors contributed equally: Zhujun Zhang, Kazuki Miyashita. ✉e-mail: tada.tomofumi.054@m.kyushu-u.ac.jp;

hosono.h.aa@m.titech.ac.jp; kitano.m.aa@m.titech.ac.jp

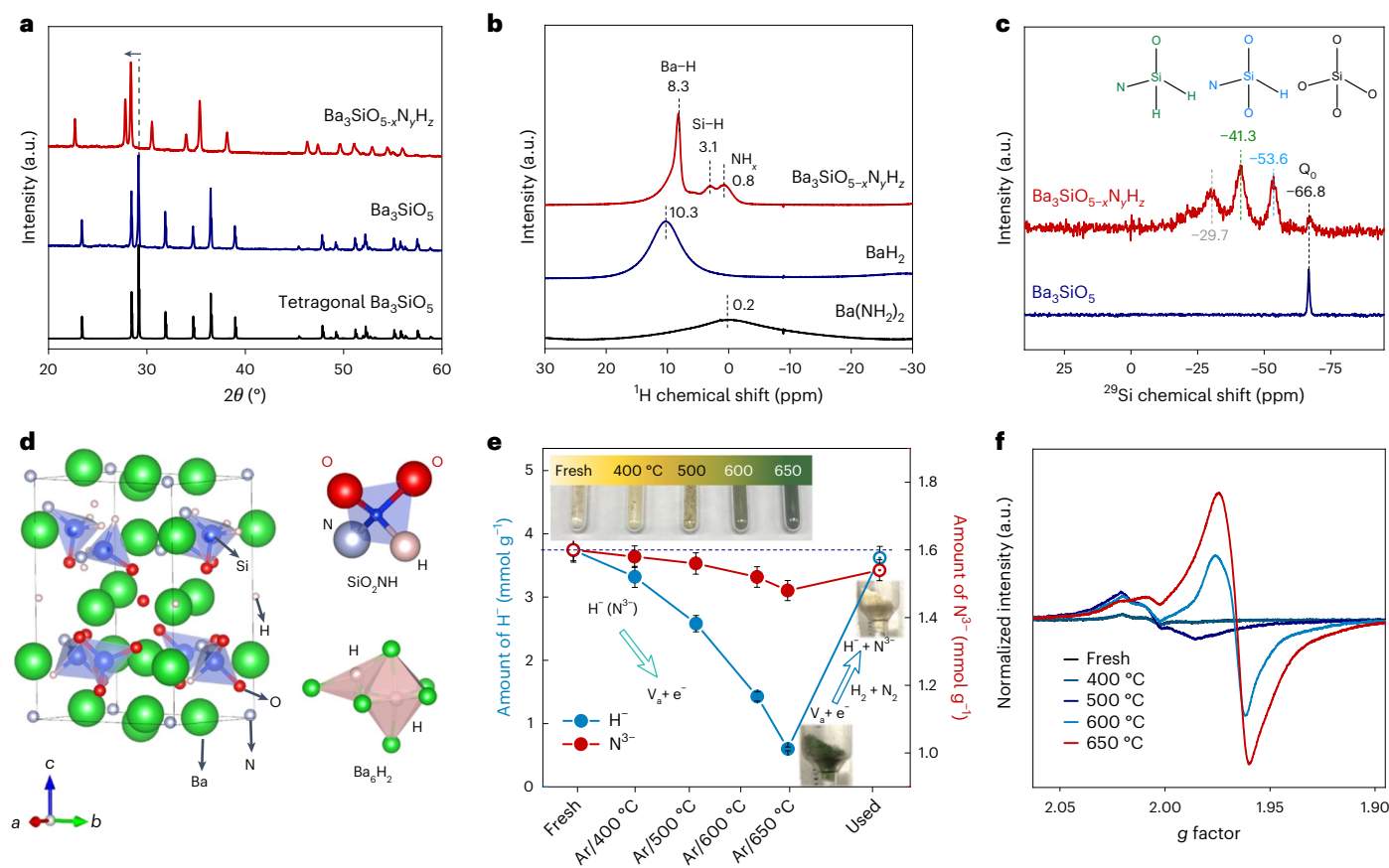


Fig. 1 | Synthesis and characterization of $\text{Ba}_3\text{SiO}_{5-x}\text{N}_y\text{H}_z$. **a**, XRD patterns of $\text{Ba}_3\text{SiO}_{5-x}\text{N}_y\text{H}_z$ and Ba_3SiO_5 . **b**, Solid-state ^1H MAS NMR spectra of $\text{Ba}_3\text{SiO}_{5-x}\text{N}_y\text{H}_z$, BaH_2 and $\text{Ba}(\text{NH}_2)_2$. **c**, Solid-state ^{29}Si MAS NMR of Ba_3SiO_5 and $\text{Ba}_3\text{SiO}_{5-x}\text{N}_y\text{H}_z$. **d**, Calculated crystal structure of $\text{Ba}_3\text{SiO}_{5-x}\text{N}_y\text{H}_z$ (left) with SiO_2NH and Ba_6H_2 blocks (right). **e**, Lattice H^- and N^{3-} contents in $\text{Ba}_3\text{SiO}_{5-x}\text{N}_y\text{H}_z$ before (fresh) and after heating in Ar at various temperatures. The used sample was obtained by heating

the sample (Ar/650 °C) under ammonia synthesis conditions (400 °C, 0.1 MPa) for 2 h. Insets: photographs of the corresponding $\text{Ba}_3\text{SiO}_{5-x}\text{N}_y\text{H}_z$ powders. The error bars represent the standard deviation of the mean based on $n = 3$ independent measurements. **f**, X-band EPR spectra of $\text{Ba}_3\text{SiO}_{5-x}\text{N}_y\text{H}_z$ before and after heating in Ar at various temperatures. a.u., arbitrary units.

(refs. 18,19). Reports on ammonia synthesis over TM-free oxide-based catalysts are lacking.

In this Article, we fabricate a Ba–Si orthosilicate oxynitride-hydride via low-temperature solid-state reaction and demonstrate its excellent ability for TM-free NH_3 synthesis under mild conditions. Although loading Ru on $\text{Ba}_3\text{SiO}_{5-x}\text{N}_y\text{H}_z$ enhances the activity, Ru does not serve to dissociate N_2 molecules but facilitates the formation of electron-containing anion vacancy (V_a) sites at the Ru–support interface. This is a striking difference from the well-known role of Ru in NH_3 synthesis. As a result, an exceptionally high ammonia synthesis rate that outperforms existing heterogeneous ammonia synthesis catalysts is realized.

Results and discussion

Synthesis and characterization of $\text{Ba}_3\text{SiO}_{5-x}\text{N}_y\text{H}_z$

The substitution of oxygen bonded to Si^{4+} with other anions is generally difficult due to the strong Si–O bonding, except under harsh conditions^{20–23}. In this Article, the following synthetic route was employed; the low-temperature (400–700 °C) solid-state reaction of $\text{Ba}(\text{NH}_2)_2$ and SiO_2 in a NH_3 flow was applied to the one-step synthesis of $\text{Ba}_3\text{SiO}_{5-x}\text{N}_y\text{H}_z$ with heavily substituted H^- and N^{3-} (Methods and Supplementary Fig. 1). The X-ray diffraction (XRD) pattern for $\text{Ba}_3\text{SiO}_{5-x}\text{N}_y\text{H}_z$ synthesized at 600 °C indicates a single Ba_3SiO_5 phase with a purity of >99% and a large shift to lower diffraction angles from that of Ba_3SiO_5 (Fig. 1 and Supplementary Fig. 2). The lattice parameters of $\text{Ba}_3\text{SiO}_{5-x}\text{N}_y\text{H}_z$ are much larger than those of Ba_3SiO_5 as determined by Rietveld fitting analysis ($\Delta V/V_0 = +9.0\%$; V and V_0 represent volume of

sample and reference Ba_3SiO_5 , respectively) (Supplementary Table 1). The H^- and N^{3-} contents of $\text{Ba}_3\text{SiO}_{5-x}\text{N}_y\text{H}_z$ were determined to be 3.74 and 1.60 mmol g^{-1} , respectively, based on temperature-programmed desorption (TPD) and an acid dissolution method (Methods), which gave the composition of $\text{Ba}_3\text{SiO}_{2.87}\text{N}_{0.80}\text{H}_{1.86}$. Diffuse reflectance spectroscopy (DRS) and projected density of states analysis of $\text{Ba}_3\text{SiO}_{5-x}\text{N}_y\text{H}_z$ suggest that the $\text{N}2p$ bands are located above the $\text{H}1s$ and $\text{O}2p$ bands and thus contribute to bandgap narrowing compared to white Ba_3SiO_5 powder (Supplementary Fig. 3).

The location of N and H in $\text{Ba}_3\text{SiO}_{5-x}\text{N}_y\text{H}_z$ has been confirmed by ^1H and ^{29}Si solid magic-angle spinning (MAS) NMR spectroscopy analysis. In the ^1H MAS NMR spectrum (Fig. 1b), the $\text{Ba}_3\text{SiO}_{5-x}\text{N}_y\text{H}_z$ sample shows a main sharp signal at 8.3 ppm. This is assigned to Ba–H species as its chemical shift is very similar to that of BaH_2 (10.3 ppm). The peaks at 3.1 and 0.8 ppm are attributed to Si–H and N–H species, respectively. The former is well consistent with H-terminated Si nanocrystals and molecular silicon hydrides (3–6 ppm)²⁴ and the latter is close to those of $\text{Ba}(\text{NH}_2)_2$ (0.2 ppm) and $\text{Ca}(\text{NH}_2)_2$ (0.7 ppm)²⁵. The N–H peak is derived from surface NH_x species on the $\text{Ba}_3\text{SiO}_{5-x}\text{N}_y\text{H}_z$ (Supplementary Fig. 4). In the ^{29}Si MAS NMR spectrum (Fig. 1c), both $\text{Ba}_3\text{SiO}_{5-x}\text{N}_y\text{H}_z$ and Ba_3SiO_5 have signals at –66.8 ppm, which are attributed to the isolated SiO_4 tetrahedra (orthosilicate anion) unit (Q_0 site). As well as this signal, new signals at –53.6, –41.3 and –29.7 ppm appeared for $\text{Ba}_3\text{SiO}_{5-x}\text{N}_y\text{H}_z$. These peaks are assignable to the Q_0 site with different anion coordinations since the ^{29}Si chemical shift tends to be more shielded with increasing group electronegativity sums of ligands

bonded to $\text{Si}^{26,27}$. Possible species are SiO_2NH , SiONH_2 and SiO_xNH_x with surface OH and/or NH species, respectively. The tetragonal Ba_3SiO_5 crystal has two types of oxygen site, that is four O_I sites in SiO_4 and one O_II site surrounded by six barium atoms (Ba_6O). Density functional theory (DFT) calculations suggest that the $\text{Ba}_3\text{SiO}_{2.5}\text{N}_{1.0}\text{H}_{2.0}$ unit cell is mainly comprised of N–H pairs that substitute two O_I sites ($2\text{O}^{2-} \Rightarrow \text{N}^{3-} + \text{H}^+$) to form SiO_2NH blocks and extra H–H pairs that substitute one O_II site ($\text{O}^{2-} \Rightarrow 2\text{H}^+$) to form Ba_6H_2 blocks (Fig. 1d and Supplementary Figs. 5 and 6). In the Ba_6H_2 block, one H^- ion is located at an O_II site and another H^- ion occupies an interstitial site adjacent to the Ba_6H_2 unit, resulting in lattice expansion ($\Delta V/V_0 = +9.4\%$, Supplementary Tables 1–4). The Ba_3SiO_5 , which is regarded as an antiperovskite, can accommodate a variety of combinations of elements because of its sufficient lattice space²⁸, enabling a unique mixed-anion structure.

The yellow-coloured $\text{Ba}_3\text{SiO}_{5-x}\text{N}_y\text{H}_z$ powder was heated under Ar gas flow to monitor the thermal stability of lattice H^- and N^{3-} . Upon increasing the temperature from 400 to 650 °C, the sample colour changed from light yellow to light green and finally to dark green (Fig. 1e). Most of the lattice H^- and a part of the N^{3-} (from the subsurface region) can be removed by heating at 650 °C in Ar flow (Fig. 1e, Supplementary Fig. 7 and Supplementary Table 5), leading to introduction of a high density of V_a sites into the crystal without destruction of the tetragonal Ba_3SiO_5 framework (Supplementary Figs. 8–11). The colour change due to the introduction of V_a sites is well understood by electron paramagnetic resonance (EPR) and DRS analysis (Fig. 1f and Supplementary Figs. 12–14). The as-prepared $\text{Ba}_3\text{SiO}_{5-x}\text{N}_y\text{H}_z$ exhibits weak EPR signals at g of approximately 2.004, 2.003 and 2.002 (Fig. 1f and Supplementary Fig. 12). The intensity of these signals was enhanced with the heating temperature and a new EPR signal at $g = 1.967$ with strong intensity appeared above 600 °C. These two sets of peaks could be attributed to the unpaired electron trapped at the V_a of the SiO_2NH and Ba_6H_2 sites. The unpaired electron density of the sample heated at 650 °C was estimated to be $1.1 \times 10^{20} \text{ cm}^{-3}$ (Supplementary Fig. 13), which is smaller than the total electron density (approximately $7.4 \times 10^{20} \text{ cm}^{-3}$) that was evaluated by the iodometric titration method²⁹. This indicates that the sample has both unpaired electrons and paired electrons in the lattice. Moreover, when the dark green $\text{Ba}_3\text{SiO}_{5-x}\text{N}_y\text{H}_z$ powder (Ar/650 °C) was heated under ammonia synthesis conditions, the lattice H^- and N^{3-} were regenerated and the dark green colour turned to the original yellow (used) (Fig. 1e).

Ammonia synthesis on $\text{Ba}_3\text{SiO}_{5-x}\text{N}_y\text{H}_z$

The fresh $\text{Ba}_3\text{SiO}_{5-x}\text{N}_y\text{H}_z$ without any TM site shows continuous ammonia production at approximately $0.37 \text{ mmol g}_{\text{cat}}^{-1} \text{ h}^{-1}$ without degradation in activity for 150 h at 400 °C and 0.9 MPa (Fig. 2a and Supplementary Table 6). The total amount of ammonia was estimated to be approximately 5.25 mmol (per 0.1 g of catalyst), which is much higher than that of the amount of lattice N^{3-} (0.16 mmol) and H^- (0.37 mmol). This indicates that the ammonia produced originates from the activation of molecular N_2 and H_2 but not from the decomposition of $\text{Ba}_3\text{SiO}_{5-x}\text{N}_y\text{H}_z$ (Supplementary Fig. 15). There was no colour change or alteration of the crystal structure after the 150 h reaction (Fig. 2b and Supplementary Figs. 8 and 9), which suggests that the $\text{Ba}_3\text{SiO}_{5-x}\text{N}_y\text{H}_z$ is chemically stable under the ammonia synthesis conditions. When the $\text{Ba}_3\text{SiO}_{5-x}\text{N}_y\text{H}_z$ was pretreated in Ar flow at 650 °C for 2 h, XRD peaks shifted towards higher angles because of removal of most lattice H^- and surface N^{3-} ions (Fig. 2b). The V_a -introduced $\text{Ba}_3\text{SiO}_{5-x}\text{N}_y\text{H}_z$ exhibited more than three times the NH_3 synthesis rate (approximately $1.20 \text{ mmol g}^{-1} \text{ h}^{-1}$) than the original one, probably due to the increase of specific surface area from 8.0 to $19.5 \text{ m}^2 \text{ g}^{-1}$. After the ammonia synthesis reaction, the V_a sites were re-occupied by H^- and N^{3-} (Supplementary Table 5), leading to a shift of XRD peaks towards the original positions and the recovery of the ^1H NMR

signal (Fig. 2b,c and Supplementary Fig. 11a). Neither white Ba_3SiO_5 , $\text{Ba}_3\text{Si}_6\text{O}_{19}\text{N}_4$, $\text{BaSi}_2\text{O}_7\text{N}_2$ or $\text{Ba}(\text{NH}_2)_2$ nor SiO_2 powder exhibits activity for ammonia synthesis, even at temperatures up to 540 °C. By contrast, the $\text{Ba}_3\text{SiO}_{5-x}\text{N}_y\text{H}_z$ powder (Ar/650 °C) can effectively activate N_2 to produce ammonia at temperatures down to 300 °C ($0.20 \text{ mmol g}^{-1} \text{ h}^{-1}$, Fig. 2d) with a low apparent activation energy (E_a) of approximately 68.5 kJ mol^{-1} , which outperforms that of the conventional Ru-loaded MgO catalyst (300 °C, $0.01 \text{ mmol g}^{-1} \text{ h}^{-1}$, $E_\text{a} = 114.5 \text{ kJ mol}^{-1}$). TPD and hydrogen temperature-programmed reduction (H_2 -TPR) analysis results show that lattice N^{3-} ions in conventional Ba–Si oxynitrides with Si–N–Si bonding are very stable and could not be reduced to ammonia up to 900 °C (Supplementary Fig. 16). This is totally different from $\text{Ba}_3\text{SiO}_{5-x}\text{N}_y\text{H}_z$. We suggest that easy thermal desorption of N^{3-} and H^- mainly comes from the orthosilicate structure of $\text{Ba}_3\text{SiO}_{5-x}\text{N}_y\text{H}_z$, where SiX_4 tetrahedra ($\text{X} = \text{O}, \text{N}, \text{H}$) do not connect with each other and lattice N and H are coordinated by not only Si but also Ba. Therefore, when the V_a sites are formed, electrons at V_a sites are stabilized by the Coulombic interaction with Ba (Fig. 2c). The lattice H^- ions do not directly contribute to hydrogenation of N_2 but provide a number of V_a sites to capture N_2 molecules in the gas phase (Supplementary Fig. 17). It can be expected that lattice H^- and N^{3-} ions are continuously exchanged with molecular H_2 and N_2 via the V_a formation on $\text{Ba}_3\text{SiO}_{5-x}\text{N}_y\text{H}_z$ during ammonia synthesis. Thus, the Ba–Si orthosilicate oxynitride-hydride was shown to function as a TM-free ammonia synthesis catalyst.

The Ru (1.5 wt%)/ $\text{Ba}_3\text{SiO}_{5-x}\text{N}_y\text{H}_z$ catalyst functioned as an efficient catalyst for ammonia synthesis at above 200 °C ($0.32 \text{ mmol g}_{\text{cat}}^{-1} \text{ h}^{-1}$) and reached $27.1 \text{ mmol g}_{\text{cat}}^{-1} \text{ h}^{-1}$ at 400 °C (Fig. 2e and Supplementary Fig. 18), which is far beyond that of the Ru/ Ba_3SiO_5 , Ru/ $\text{Ba}_3\text{Si}_6\text{O}_{19}\text{N}_4$ and Ru/ $\text{BaSi}_2\text{O}_7\text{N}_2$ catalysts. The high ammonia synthesis activity was maintained for more than 170 h without crystal structure decomposition (Supplementary Fig. 19 and Supplementary Table 5), which demonstrates its excellent catalytic stability. This result is in contrast to that of the reported TM-free catalyst, potassium hydride-intercalated graphite composite catalyst ($\text{KH}_{0.19}\text{C}_{24}$). The activity of $\text{KH}_{0.19}\text{C}_{24}$ is not promoted by the supported TM catalysts⁹. The E_a of Ru/ $\text{Ba}_3\text{SiO}_{5-x}\text{N}_y\text{H}_z$ was as low as 64.4 kJ mol^{-1} , which is much lower than that of Ru/ Ba_3SiO_5 ($110.3 \text{ kJ mol}^{-1}$) and the reported conventional Ru-based catalysts (85 – 121 kJ mol^{-1}). When Ru/ $\text{Ba}_3\text{SiO}_{5-x}\text{N}_y\text{H}_z$ particles (Ru: 1.5 wt%) were dispersed on the SiO_2 surface, the resultant sample ($\text{Ba}_3\text{SiO}_{5-x}\text{N}_y\text{H}_z/\text{HS}$) with high surface area ($105 \text{ m}^2 \text{ g}^{-1}$) (Supplementary Fig. 20) exhibited much higher catalytic performance than that of Ru/ $\text{Ba}_3\text{SiO}_{5-x}\text{N}_y\text{H}_z$. After the optimization of the reaction conditions (Supplementary Fig. 21), Ru (5.0 wt%)/ $\text{Ba}_3\text{SiO}_{5-x}\text{N}_y\text{H}_z/\text{HS}$ recorded the highest ammonia synthesis rate among the reported catalysts (Fig. 2f and Supplementary Table 7)^{12,15,16,30–33}. In addition, the activity of Ru/ $\text{Ba}_3\text{SiO}_{5-x}\text{N}_y\text{H}_z/\text{HS}$ was maintained even after exposure to air for 2 h (Supplementary Fig. 22). The excess SiO_2 may improve the stability of the catalyst in air.

High-angle annular dark-field scanning transmission electron microscopy (HAADF-STEM) analysis showed that small-sized Ru nanoparticles (approximately 3 nm) are highly dispersed on the surface of $\text{Ba}_3\text{SiO}_{5-x}\text{N}_y\text{H}_z$ (Supplementary Fig. 23). The Ru particle size of Ru/ $\text{Ba}_3\text{SiO}_{5-x}\text{N}_y\text{H}_z$ is smaller than that of Ru/ Ba_3SiO_5 , while the large activity difference between them cannot be explained by the Ru particle size. For Ru/ $\text{Ba}_3\text{SiO}_{5-x}\text{N}_y\text{H}_z/\text{HS}$, the $\text{Ba}_3\text{SiO}_{5-x}\text{N}_y\text{H}_z$ particles with sizes of 100–200 nm are dispersed on the surface of SiO_2 (Fig. 2g and Supplementary Fig. 24). As a result, the active $\text{Ba}_3\text{SiO}_{5-x}\text{N}_y\text{H}_z$ loaded with tiny Ru nanoparticles (approximately 2.5 nm) is effectively exposed on the catalyst surface for Ru/ $\text{Ba}_3\text{SiO}_{5-x}\text{N}_y\text{H}_z/\text{HS}$. The valance state of Ru on $\text{Ba}_3\text{SiO}_{5-x}\text{N}_y\text{H}_z$ is almost neutral (metallic) but slightly positive according to the Ru K-edge X-ray absorption near edge structure (XANES) (Supplementary Fig. 25) and X-ray photoelectron spectroscopy (XPS) results (Supplementary Fig. 26). This suggests that the electrons are donated from Ru to $\text{Ba}_3\text{SiO}_{5-x}\text{N}_y\text{H}_z$ due to the strong Ru–N interaction. This result is rather different from those of conventional

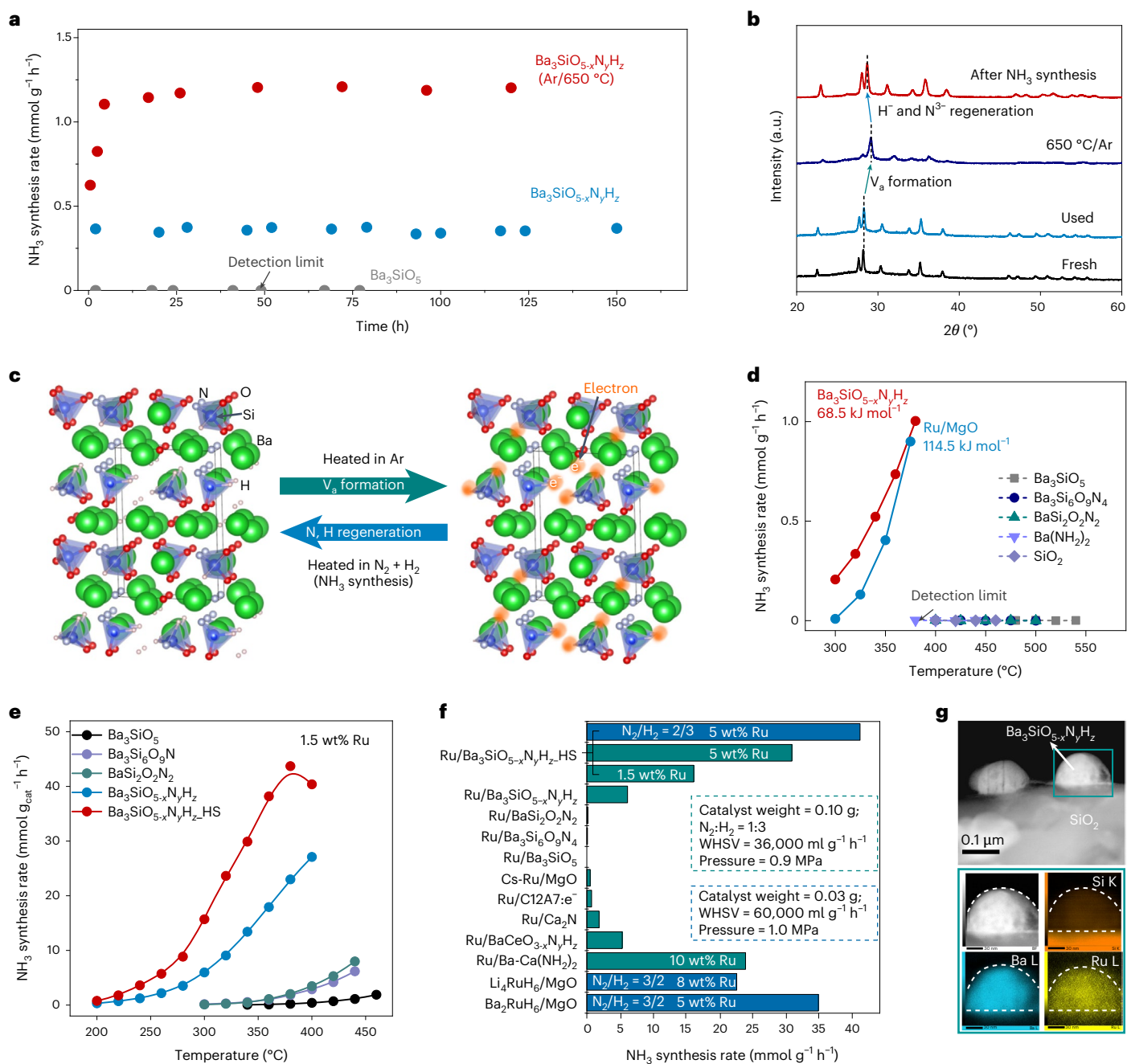


Fig. 2 | Ammonia synthesis on $\text{Ba}_3\text{SiO}_{5-x}\text{N}_y\text{H}_z$. **a**, Time courses for ammonia synthesis over as-prepared $\text{Ba}_3\text{SiO}_{5-x}\text{N}_y\text{H}_z$, $\text{Ba}_3\text{SiO}_{5-x}\text{N}_y\text{H}_z$ pretreated at 650 °C in Ar for 2 h and Ba_3SiO_5 at 400 °C and 0.9 MPa. **b**, XRD patterns of as-prepared $\text{Ba}_3\text{SiO}_{5-x}\text{N}_y\text{H}_z$ (fresh) and $\text{Ba}_3\text{SiO}_{5-x}\text{N}_y\text{H}_z$ pretreated at 650 °C in Ar for 2 h before and after the catalytic test in a. **c**, Schematic illustration of thermal induced V_a and electron formation and the N, H regeneration under NH_3 synthesis

conditions in $\text{Ba}_3\text{SiO}_{5-x}\text{N}_y\text{H}_z$. **d, e**, Temperature dependence of the NH_3 synthesis rate over TM-free materials (**d**) and the Ru (1.5 wt%) loaded samples under a pressure of 0.9 MPa (**e**). **f**, NH_3 synthesis rates for various Ru-based catalysts at 300 °C. **g**, HAADF-STEM image (top) and EDX-mapping (bottom) of used $\text{Ru/Ba}_3\text{SiO}_{5-x}\text{N}_y\text{H}_z\text{-HS}$.

Ru-based ammonia synthesis catalysts that require negatively charged Ru to activate N_2 . The reaction orders of N_2 (α), H_2 (β) and NH_3 (γ) for $\text{Ru/Ba}_3\text{SiO}_{5-x}\text{N}_y\text{H}_z$ were determined to be 0.55, 0.48 and -0.63 , respectively (Supplementary Fig. 27). In particular, the N_2 reaction order ($\alpha = +0.55$) is only half that of conventional catalysts ($\alpha = -1.0$), where the overall reaction rate is limited by the N_2 cleavage step. This result indicates the change of RDS from N_2 dissociation to other elementary steps over the $\text{Ru/Ba}_3\text{SiO}_{5-x}\text{N}_y\text{H}_z$ catalyst. The H_2 reaction order for $\text{Ru/Ba}_3\text{SiO}_{5-x}\text{N}_y\text{H}_z$ is positive ($\beta = +0.48$), which suggests that the $\text{Ru/Ba}_3\text{SiO}_{5-x}\text{N}_y\text{H}_z$ is not subject to H_2 poisoning.

Isotope-labelled ammonia synthesis on $\text{Ba}_3\text{SiO}_{5-x}\text{N}_y\text{H}_z$
Ammonia synthesis employing a mixed gas flow of $^{15}\text{N}_2$ and H_2 at 400 °C was conducted to elucidate the catalytic reaction mechanism over $\text{Ba}_3\text{SiO}_{5-x}\text{N}_y\text{H}_z$ and $\text{Ru/Ba}_3\text{SiO}_{5-x}\text{N}_y\text{H}_z$. The $m/z = 16, 17$ and 18 signals gradually increased with decreasing $m/z = 30$ ($^{15}\text{N}_2$) and $m/z = 2$ (H_2) (Supplementary Figs. 28 and 29), which indicates the effective formation of ammonia over $\text{Ba}_3\text{SiO}_{5-x}\text{N}_y\text{H}_z$ in the absence of any TM sites (Fig. 3a). No $^{29}\text{N}_2$ formation indicates that the N_2 isotope exchange reaction (N_2 -IER) does not proceed since the $\text{Ba}_3\text{SiO}_{5-x}\text{N}_y\text{H}_z$ does not have direct N_2 dissociation ability. In contrast to Ru/MgO

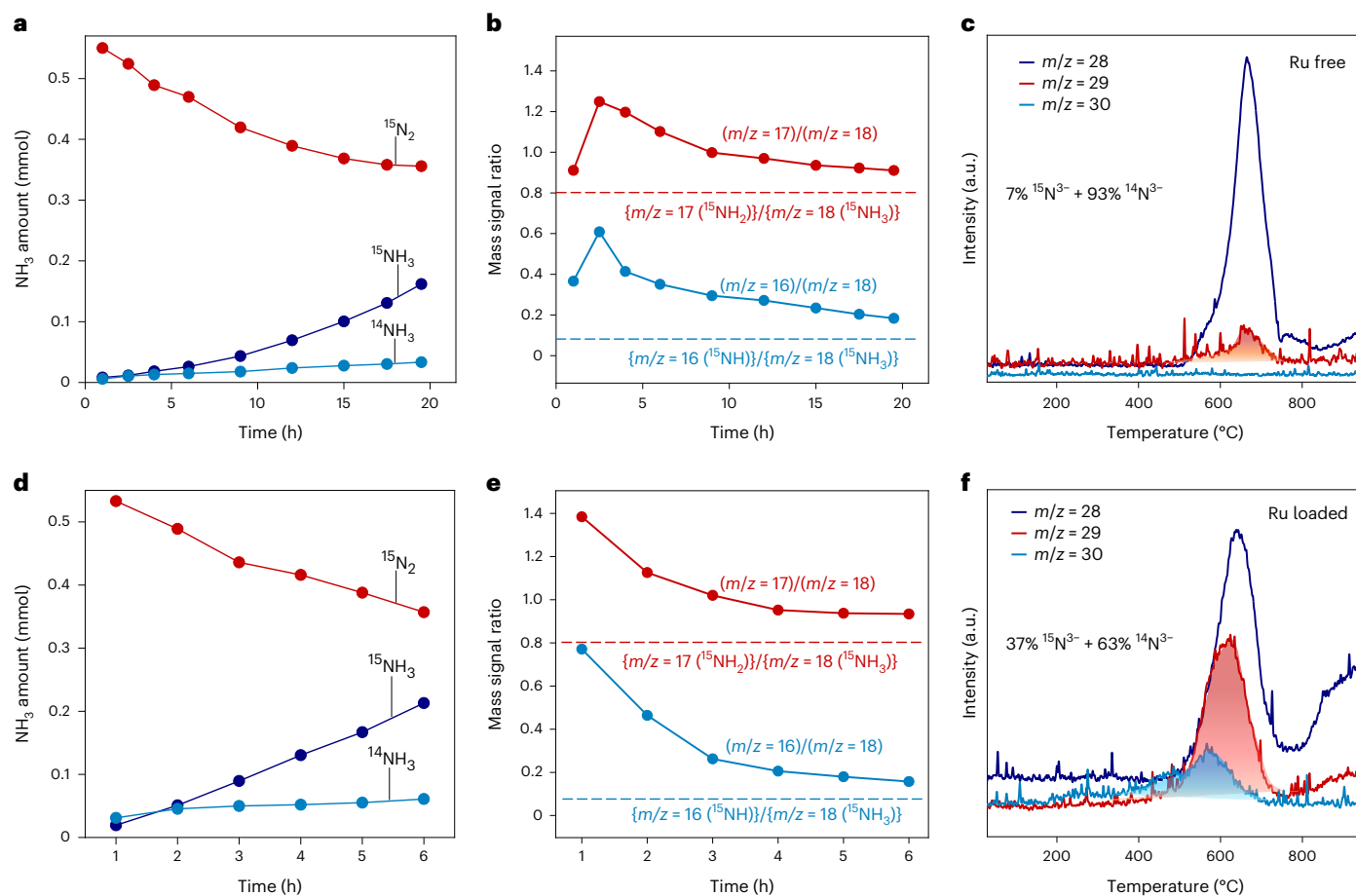


Fig. 3 | Isotope-labelled ammonia synthesis on $\text{Ba}_3\text{SiO}_{5-x}\text{N}_y\text{H}_z$. **a, b,** Reaction time profiles for NH_3 synthesis from $^{15}\text{N}_2$ and H_2 over $\text{Ba}_3\text{SiO}_{5-x}\text{N}_y\text{H}_z$ (**a**) and the change in mass signal ratio over reaction time (**b**). **c,** TPD for $\text{Ba}_3\text{SiO}_{5-x}\text{N}_y\text{H}_z$ collected after the isotope-labelled ammonia synthesis. **d, e,** Reaction time profiles for NH_3 synthesis from $^{15}\text{N}_2$ and H_2 over $\text{Ru}/\text{Ba}_3\text{SiO}_{5-x}\text{N}_y\text{H}_z$ (**d**) and the

change in mass signal ratio over reaction time (**e**). The dotted lines in **b** and **e** represent the theoretical fragment ratio ($\text{NH}_2/\text{NH}_3 = 0.8$ and $\text{NH}/\text{NH}_3 = 0.075$). **f,** TPD for $\text{Ru}/\text{Ba}_3\text{SiO}_{5-x}\text{N}_y\text{H}_z$ collected after the isotope-labelled ammonia synthesis. The content of ^{15}N in the desorbed nitrogen gas was calculated from the shaded area in panels **c** and **f**.

(Supplementary Fig. 30), the mass signal intensity ratios of $(m/z = 16)/(m/z = 18)$ and $(m/z = 17)/(m/z = 18)$ over $\text{Ba}_3\text{SiO}_{5-x}\text{N}_y\text{H}_z$ were much larger than the theoretical values of 0.8 and 0.075 (Fig. 3b), which indicates the formation of $^{15}\text{NH}_3$ as well as $^{14}\text{NH}_3$. N_2 gas with ^{15}N was desorbed from the $\text{Ba}_3\text{SiO}_{5-x}\text{N}_y\text{H}_z$ used after the isotope-labelled ammonia synthesis test (Fig. 3c), indicating that lattice $^{14}\text{N}^{3-}$ of $\text{Ba}_3\text{SiO}_{5-x}\text{N}_y\text{H}_z$ was partially replaced with $^{15}\text{N}^{3-}$ from gaseous $^{15}\text{N}_2$ during the isotope test. Similar results were observed for $\text{Ru}/\text{Ba}_3\text{SiO}_{5-x}\text{N}_y\text{H}_z$ (Fig. 3d–f and Supplementary Fig. 31), which suggests the Ru-loading does not change the V_a -mediated N_2 activation processes. The concentration of lattice $^{15}\text{N}^{3-}$ in $\text{Ru}/\text{Ba}_3\text{SiO}_{5-x}\text{N}_y\text{H}_z$ reaches approximately 37%, which is more than five times higher than that of bare $\text{Ba}_3\text{SiO}_{5-x}\text{N}_y\text{H}_z$ (approximately 7%) and illustrates that loading of Ru nanoparticles would facilitate the formation of V_a sites at the Ru–support interface as N_2 activation centres. The catalytic cycle for V_a -mediated N_2 activation to ammonia was further confirmed by switching the reaction gas atmosphere between H_2 and N_2 (Supplementary Fig. 32). Accordingly, the lattice N^{3-} ions in $\text{Ba}_3\text{SiO}_{5-x}\text{N}_y\text{H}_z$ were consumed by hydrogenation and were immediately regenerated by the reaction of V_a sites with molecular N_2 . This shows that the transiently formed V_a sites function for N_2 activation. To confirm the validity of this model, we examined the effect of Ni (which is known to have weak interaction with N) loading, and found no significant enhancement of activity ($2.1 \text{ mmol g}^{-1} \text{ h}^{-1}$ at $400 ^{\circ}\text{C}$ and 0.9 MPa) and V_a formation compared with the bare $\text{Ba}_3\text{SiO}_{5-x}\text{N}_y\text{H}_z$ (Supplementary Figs. 33 and 34).

Anion-vacancy-mediated N_2 activation on $\text{Ba}_3\text{SiO}_{5-x}\text{N}_y\text{H}_z$
 N_2 activation on the $\text{Ba}_3\text{SiO}_{5-x}\text{N}_y\text{H}_z$ catalyst was further examined using diffuse-reflectance infrared Fourier transform spectroscopy (DRIFTS). It should be noted that $\text{Ba}_3\text{SiO}_{5-x}\text{N}_y\text{H}_z$ without Ru exhibits a peak centred at around $2,016 \text{ cm}^{-1}$, which is much lower than that of conventional Ru catalysts (Ru/MgO , $2,231 \text{ cm}^{-1}$)^{34,35} and electrode-based catalysts ($\text{Ru}/\text{Cl}_2\text{A}7\text{:e}^-$, $2,176 \text{ cm}^{-1}$)¹² (Fig. 4a and Supplementary Fig. 35). This is in contrast to N_2 adsorption on conventional non-TM sites through electrostatic interaction, where N_2 serves as a weak base molecule interacting with acid sites (electropositive sites) resulting in a blue-shift of the $\text{N}=\text{N}$ bond frequency^{36–38}. In the case of $\text{Ba}_3\text{SiO}_{5-x}\text{N}_y\text{H}_z$, electrons trapped at the V_a sites directly interact with N_2 and facilitate π backdonation into the antibonding orbital of the N_2 molecule, which leads to a red-shift of the N_2 adsorption band. The N_2 peak position slightly blue-shifts after Ru loading on the $\text{Ba}_3\text{SiO}_{5-x}\text{N}_y\text{H}_z$ surface, which indicates that N_2 molecules are mainly captured at the V_a sites of $\text{Ba}_3\text{SiO}_{5-x}\text{N}_y\text{H}_z$ accompanied by the influence of the positively charged Ru site. The N_2 -IER rate of $\text{Ru}/\text{Ba}_3\text{SiO}_{5-x}\text{N}_y\text{H}_z$ is negligibly smaller than that of Ru/MgO although $\text{Ru}/\text{Ba}_3\text{SiO}_{5-x}\text{N}_y\text{H}_z$ showed an over ten times higher ammonia synthesis rate than Ru/MgO (Fig. 4b and Supplementary Fig. 36). This result indicates that the Ru nanoparticles on $\text{Ba}_3\text{SiO}_{5-x}\text{N}_y\text{H}_z$ do not function to dissociate N_2 , which is a striking difference from the well-known role of Ru in NH_3 synthesis^{39–41}.

In situ DRIFTS measurements (Fig. 4c and Supplementary Fig. 37) showed N_2 adsorption peaks at $2,161$ and $1,976 \text{ cm}^{-1}$, which may be

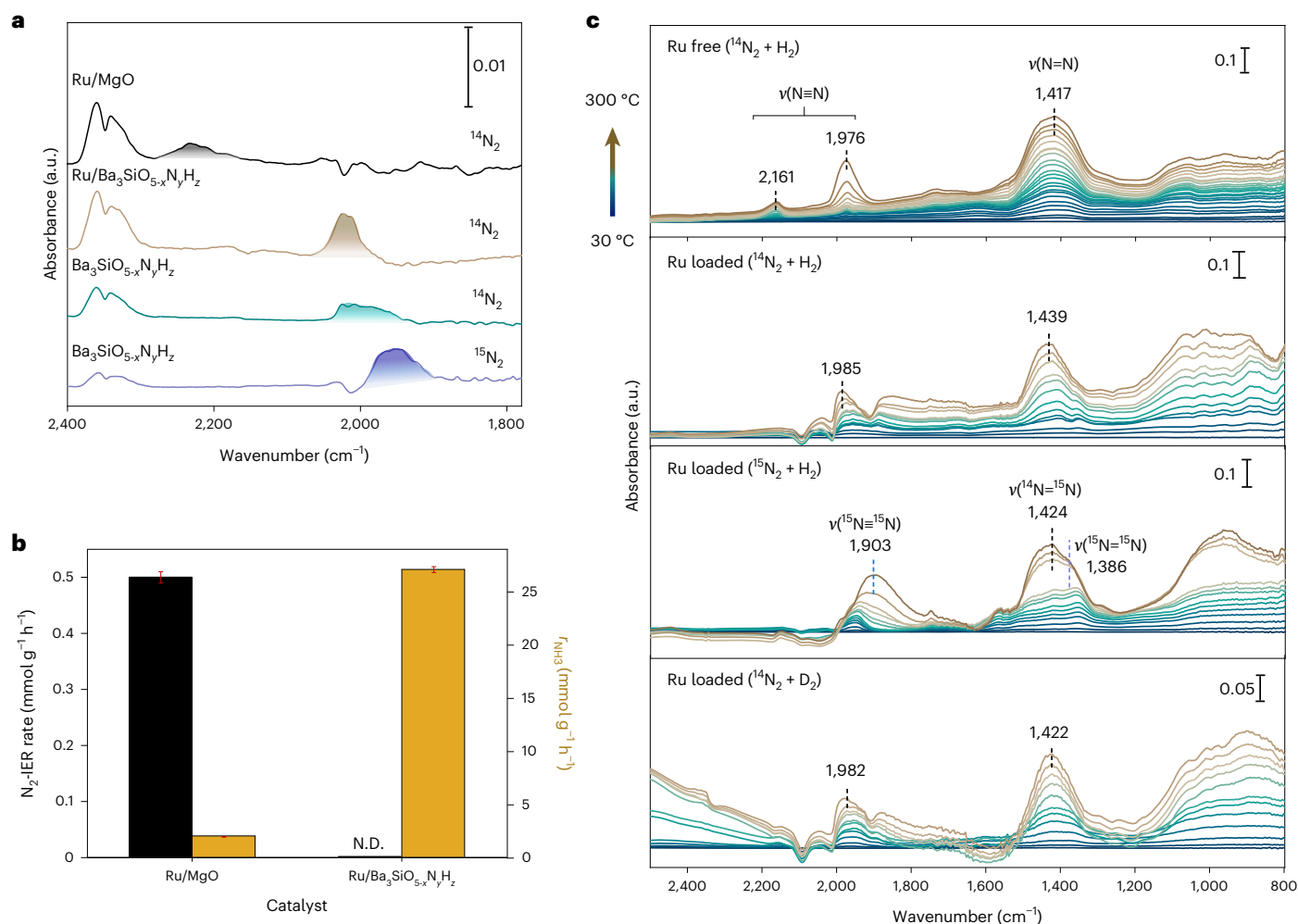


Fig. 4 | Anion-vacancy-mediated N₂ activation on Ba₃SiO_{5-x}N_yH_z. **a**, DRIFTS N₂ adsorption on Ru/MgO, Ru/Ba₃SiO_{5-x}N_yH_z and Ba₃SiO_{5-x}N_yH_z at -170 °C. **b**, Comparison of N₂-IER rate and ammonia synthesis rate (0.9 MPa) at 400 °C for Ru/MgO and Ru/Ba₃SiO_{5-x}N_yH_z. The error bars represent the standard deviation

attributed to N≡N stretching of N₂ molecules adsorbed at different V_a sites close to Si and Ba sites on Ba₃SiO_{5-x}N_yH_z. In particular, the latter peak was red-shifted relative to that observed at -170 °C (2,016 cm⁻¹). This means that the N≡N bond is effectively weakened at reaction temperatures⁴². In addition, the peak intensity steeply increased with increasing reaction temperature especially above 200 °C. This is due to the accumulation of N₂ molecules at the V_a sites not only on the top surface but also in the subsurface region of Ba₃SiO_{5-x}N_yH_z. It should be noted that another intense band was observed at approximately 1,417 cm⁻¹, which can be assigned to the N=N bond⁴³. Moreover, the N-H stretching vibration was observed at 3,187–3,244 cm⁻¹ (Supplementary Fig. 37b), which is attributed to the formation of imide species. Similar intermediates were observed for Ru/Ba₃SiO_{5-x}N_yH_z, where N₂ peaks above 2,000 cm⁻¹ are immediately consumed to form other nitrogen species, giving negative peaks. Accordingly, NNH species could be generated as intermediates on this catalyst during ammonia synthesis. The N≡N (1,985 cm⁻¹) and N=N (1,439 cm⁻¹) stretching vibration of Ru/Ba₃SiO_{5-x}N_yH_z red-shifted to 1,903 cm⁻¹ and 1,386 cm⁻¹, respectively when ¹⁵N₂ and H₂ flow was conducted (Fig. 4c). The peak shift is reasonably explained by the isotope effect (1,985 cm⁻¹ × (14/15)^{1/2} = 1,917 cm⁻¹, 1,439 cm⁻¹ × (14/15)^{1/2} = 1,390 cm⁻¹). The 1,439 cm⁻¹ peak is not due to the H-N-H bending vibration since the peak position is not largely shifted under ¹⁴N₂ and D₂ flow conditions. On the other hand, the NNH bending vibration would appear at around 1,400–1,480 cm⁻¹, overlapping with

of the mean based on *n* = 3 independent measurements. N.D., not detected. **c**, In situ DRIFTS observation of formation of intermediates on Ba₃SiO_{5-x}N_yH_z (Ru free) and Ru/Ba₃SiO_{5-x}N_yH_z (Ru loaded). The measurement temperature was increased from 30 °C (blue) to 300 °C (brown).

the broad ν(N=N) band centred at around 1,420 cm⁻¹. The small shift from 1,439 to 1,422 cm⁻¹ is consistent with the isotope effect from the N=N bond in NNH (1,439 cm⁻¹) to NND (1,417 cm⁻¹). From these results, it can be concluded that the N₂ molecule is activated at V_a sites on Ba₃SiO_{5-x}N_yH_z and sequentially hydrogenated to form NNH_x (*x* = 1–3) species through the associative reaction mechanism.

DFT calculations

A DFT calculation study of reaction pathways was performed using Ba₄₈Si₁₆O₄₀N₁₅H₃₂ loaded with Ru₁₂ clusters and the reference Ru/MgO catalyst (Fig. 5 and Supplementary Figs. 38 and 39). First, H₂ was dissociated on Ru with a negligible energy barrier (I → II). The dissociated H* was then migrated from the Ru surface to a nearby lattice N of the support (II → III). Further hydrogenation reactions occurred sequentially to form NH₃ and a nitrogen vacancy site (V_N) site was formed after NH₃ desorption (III → VII). The formation energy of an N vacancy (E_{NV} of Ru/Ba₃SiO_{5-x}N_yH_z (-1.21 eV) is much lower than that of bare Ba₃SiO_{5-x}N_yH_z (-0.87 eV), which indicates that the supported Ru nanoparticles facilitate the formation of V_N sites (Supplementary Fig. 40). The adsorption energies of N₂ on both Ru and V_N sites of Ru/Ba₃SiO_{5-x}N_yH_z are calculated to be -0.4 eV (Supplementary Fig. 41), suggesting that N₂ is likely to be adsorbed on both sites. The energy barrier for N₂ dissociation on the Ru surface was 0.47 eV, which was lower than that of NNH formation (0.79 eV, TS IV). However, CO adsorption experiments confirmed that

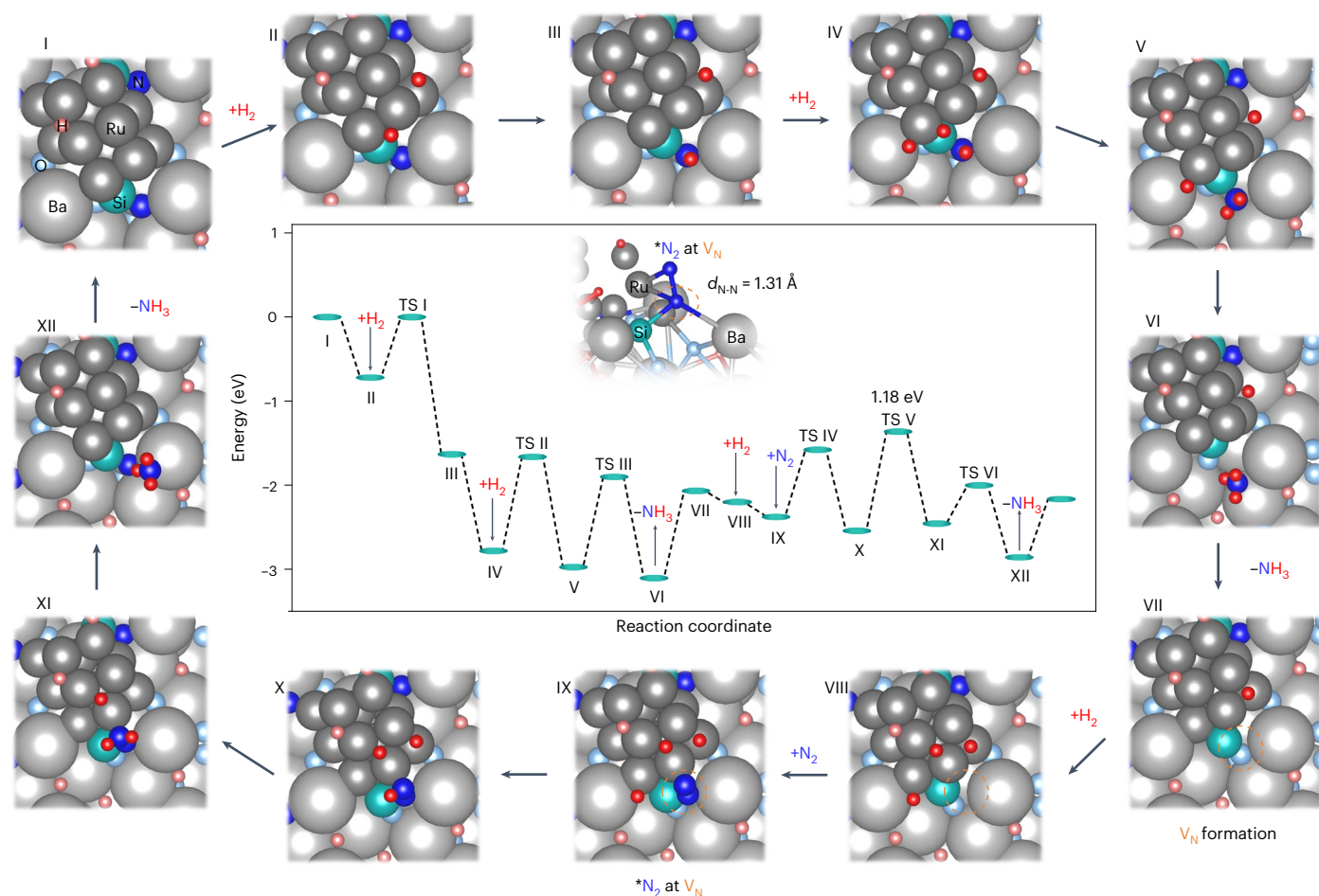


Fig. 5 | DFT calculations. The proposed reaction pathway for V_N -mediated ammonia synthesis on the $Ru/Ba_3SiO_{5-x}N_yH_z$ surface. The central plot shows the energy profiles determined from DFT calculations. TS, transition state.

The structures of reaction intermediates on $Ru_{12}/Ba_{48}Si_{16}O_{40}N_{15}H_{32}$ for each elementary step (I–XII) are shown around the outside of the central plot. The structure of $*N_2$ adsorbed on the V_N site is highlighted in the central plot.

the Ru surface was barely exposed on $Ru/Ba_3SiO_{5-x}N_yH_z$ (Supplementary Fig. 42). Therefore, the N_2 activation at the V_N site is more plausible than that on the Ru surface. The N_2 molecule adsorbed at the V_N site was coordinated to the adjacent Ba, Si and Ru sites, resulting in elongation of the N–N bond (1.31 Å) (Step IX). The hydrogenation of N_2 at the V_N site to form $*NNH$ (IX \rightarrow X) occurs in preference to direct dissociation of N_2 (Supplementary Fig. 43). $*NNH_2$ and $*NNH_3$ are generated by sequential hydrogenation (VIII \rightarrow XII) via the distal pathway⁴⁴. The energy barriers for the hydrogenation of both lattice N and molecular N_2 are similar, in the range 0.44–1.18 eV, indicating that these hydrogenation steps are kinetically significant. Among them, the step for $*NNH$ to $*NNH_2$ (1.18 eV) is the highest and is considered as the RDS. These calculation results agree well with the in situ DRIFTS observation result as shown in Fig. 4c, in which the NNH species is the main intermediate on the $Ru/Ba_3SiO_{5-x}N_yH_z$ catalyst. After NH_3 desorption from NNH_3 , the remaining nitrogen compensates the V_N site to restore the initial $Ba_3SiO_{5-x}N_yH_z$ surface. The lattice hydrogen on $Ba_3SiO_{5-x}N_yH_z$ easily migrates and covers the Ru surface (I in Fig. 5) and hydrogen is rapidly transferred to the Ru surface even when the H_2 molecule is adsorbed on the V_N site (Supplementary Fig. 44). These results support our proposed reaction mechanism, in which N_2 and H_2 molecules are activated at the V_N site and Ru surface, respectively.

Conclusion

In summary, we employed a low-temperature solid-state reaction strategy for the synthesis of a Ba–Si orthosilicate oxynitride-hydride with a high concentration of lattice H^- and N^{3-} heteroanions. The anion

vacancy of this TM-free oxide-based compound serves as an active site for efficient N_2 activation and hydrogenation to ammonia. The ammonia synthesis rate is dramatically increased upon Ru loading (1.5–5.0 wt%), where Ru does not work to dissociate N_2 but facilitates the formation of V_N sites at the Ru–support interface. Isotope-labelling ammonia synthesis, N_2 exchange and DRIFTS N_2 adsorption experiments showed that N_2 molecules are directly activated by the electron-containing V_N sites of Ba–Si orthosilicate oxynitride-hydride and thus facilitate ammonia synthesis via hydrogenation processes with low activation barriers. We suggest that easy formation of V_N sites and the flexibility of the crystal structure that allows it to accommodate large amounts of anion vacancies are essential to enable the higher catalytic activity. Our studies of V_N -mediated dinitrogen reduction to ammonia over this oxynitride-hydride catalyst illustrate the significant potential for the development of more efficient catalysts for low-temperature ammonia synthesis and other heterogeneous catalysis processes.

Online content

Any methods, additional references, Nature Portfolio reporting summaries, source data, extended data, supplementary information, acknowledgements, peer review information; details of author contributions and competing interests; and statements of data and code availability are available at <https://doi.org/10.1038/s41557-025-01737-8>.

References

1. Mars, P. & van Krevelen, D. W. Oxidations carried out by means of vanadium oxide catalysts. *Chem. Eng. Sci.* **3**, 41–59 (1954).

2. Widmann, D. & Behm, R. J. Activation of molecular oxygen and the nature of the active oxygen species for CO oxidation on oxide supported Au catalysts. *Acc. Chem. Res.* **47**, 740–749 (2014).
3. Yoon, B. et al. Charging effects on bonding and catalyzed oxidation of CO on Au₈ clusters on MgO. *Science* **307**, 403–407 (2005).
4. Ye, T. N. et al. Vacancy-enabled N₂ activation for ammonia synthesis on an Ni-loaded catalyst. *Nature* **583**, 391–395 (2020).
5. van Ommen, J. G., Bolink, W. J., Prasad, J. & Mars, P. The nature of the potassium compound acting as a promoter in iron–alumina catalysts for ammonia synthesis. *J. Catal.* **38**, 120–127 (1975).
6. Deinalipour-Yazdi, C. D. et al. Nitrogen activation in a Mars–van Krevelen mechanism for ammonia synthesis on Co₃Mo₃N. *J. Phys. Chem. C* **119**, 28368–28376 (2015).
7. Nørskov, J. K., Bligaard, T., Rossmeisl, J. & Christensen, C. H. Towards the computational design of solid catalysts. *Nat. Chem.* **1**, 37–46 (2009).
8. Ozaki, A. Development of alkali-promoted ruthenium catalyst for ammonia synthesis. *Acc. Chem. Res.* **14**, 16–21 (1981).
9. Bielawa, H., Hinrichsen, O., Birkner, A. & Muhler, M. The ammonia-synthesis catalyst of the next generation: barium-promoted oxide-supported ruthenium. *Angew. Chem. Int. Ed.* **40**, 1061–1063 (2001).
10. Hosono, H. & Kitano, M. Advances in materials and applications of inorganic electrides. *Chem. Rev.* **121**, 3121–3185 (2021).
11. Matsuishi, S. et al. High-density electron anions in a nanoporous single crystal: [Ca₂₄Al₂₈O₆₄]⁴⁺ (4e[−]). *Science* **301**, 626–629 (2003).
12. Kitano, M. et al. Ammonia synthesis using a stable electride as an electron donor and reversible hydrogen store. *Nat. Chem.* **4**, 934–940 (2012).
13. Inoue, Y. et al. Direct activation of cobalt catalyst by 12CaO·7Al₂O₃ electride for ammonia synthesis. *ACS Catal.* **9**, 1670–1679 (2019).
14. Wang, P. et al. Breaking scaling relations to achieve low-temperature ammonia synthesis through LiH-mediated nitrogen transfer and hydrogenation. *Nat. Chem.* **9**, 64–70 (2017).
15. Wang, Q. et al. Ternary ruthenium complex hydrides for ammonia synthesis via the associative mechanism. *Nat. Catal.* **4**, 959–967 (2021).
16. Kitano, M. et al. Low-temperature synthesis of perovskite oxynitride-hydrides as ammonia synthesis catalysts. *J. Am. Chem. Soc.* **141**, 20344–20353 (2019).
17. Kobayashi, Y. et al. Titanium-based hydrides as heterogeneous catalysts for ammonia synthesis. *J. Am. Chem. Soc.* **139**, 18240–18246 (2017).
18. Guan, Y. et al. Transition-metal-free barium hydride mediates dinitrogen fixation and ammonia synthesis. *Angew. Chem. Int. Ed.* **61**, e2022058 (2022).
19. Chang, F. et al. Potassium hydride-intercalated graphite as an efficient heterogeneous catalyst for ammonia synthesis. *Nat. Catal.* **5**, 222–230 (2022).
20. Schlenz, H. et al. Structure analyses of Ba-silicate glasses. *J. Non. Cryst. Solids* **297**, 37–54 (2002).
21. Mishra, L. et al. White light emission and color tunability of dysprosium doped barium silicate glasses. *J. Lumin.* **169**, 121–127 (2016).
22. Wusirika, R. Reaction of ammonia with fumed silica. *J. Am. Ceram. Soc.* **73**, 2926–2929 (1990).
23. Wang, M. et al. Long-lasting phosphorescence in BaSi₂O₂N₂:Eu²⁺ and Ba₂SiO₄:Eu²⁺ phases for X-ray and cathode ray tubes. *J. Electrochem. Soc.* **157**, H178 (2010).
24. Hanrahan, M. P. et al. Characterization of silicon nanocrystal surfaces by multidimensional solid-state NMR spectroscopy. *Chem. Mater.* **29**, 10339–10351 (2017).
25. Hayashi, F. et al. NH₂^{2−} dianion entrapped in a nanoporous 12CaO·7Al₂O₃ crystal by ammonothermal treatment: reaction pathways, dynamics, and chemical stability. *J. Am. Chem. Soc.* **136**, 11698–11706 (2014).
26. Janes, N. & Oldfield, E. Prediction of silicon-29 nuclear magnetic resonance chemical shifts using a group electronegativity approach: applications to silicate and aluminosilicate structures. *J. Am. Chem. Soc.* **107**, 6769–6775 (1985).
27. Van Weeren, R. et al. Synthesis and characterization of amorphous Si₃N₂O. *J. Am. Ceram. Soc.* **77**, 2699–2702 (1994).
28. Mutschke, A. et al. Expanding the hydride chemistry: antiperovskites A₃MO₄H (A = Rb, Cs; M = Mo, W) introducing the transition oxometalate hydrides. *Chem. Sci.* **13**, 7773–7779 (2022).
29. Yoshizumi, T., Matsuishi, S., Kim, S. W., Hosono, H. & Hayashi, K. Iodometric determination of electrons incorporated into cages in 12CaO·7Al₂O₃ crystals. *J. Phys. Chem. C* **114**, 15354–15357 (2010).
30. Kitano, M. et al. Self-organized ruthenium–barium core–shell nanoparticles on a mesoporous calcium amide matrix for efficient low-temperature ammonia synthesis. *Angew. Chem. Int. Ed.* **57**, 2648–2652 (2018).
31. Hattori, M. et al. Enhanced catalytic ammonia synthesis with transformed BaO. *ACS Catal.* **8**, 10977–10984 (2018).
32. Sato, K. et al. Surface dynamics for creating highly active Ru sites for ammonia synthesis: accumulation of a low-crystalline, oxygen-deficient nanofraction. *ACS Sustain. Chem. Eng.* **8**, 2726–2734 (2020).
33. Kitano, M. et al. Essential role of hydride ion in ruthenium-based ammonia synthesis catalysts. *Chem. Sci.* **7**, 4036–4043 (2016).
34. Kubota, J. & Aika, K. I. Infrared spectra of adsorbed dinitrogen on ruthenium metal supported on alumina and magnesium oxide. *J. Chem. Soc. Chem. Commun.* **2**, 1544–1545 (1991).
35. Kubota, J. & Aika, K. I. Infrared studies of adsorbed dinitrogen on supported ruthenium catalysts for ammonia synthesis. Effects of the alumina and magnesia supports and the cesium compound promoter. *J. Phys. Chem.* **98**, 11293–11300 (1994).
36. Groppo, E. et al. FTIR investigation of the H₂, N₂, and C₂H₄ molecular complexes formed on the Cr(II) sites in the Phillips catalyst: a preliminary step in the understanding of a complex system. *J. Phys. Chem. B* **109**, 15024–15031 (2005).
37. Bulanin, K. M., Lobo, R. F. & Bulanin, M. O. Low-temperature adsorption of N₂, O₂, and D₂ on LiX, NaX, and NaLiX zeolites studied by FT-IR spectroscopy. *J. Phys. Chem. B* **104**, 1269–1276 (2000).
38. Wakabayashi, F., Kondo, J., Wada, A., Domen, K. & Hirose, C. FT-IR studies of the interaction between zeolitic hydroxyl groups and small molecules. 1. Adsorption of nitrogen on H-mordenite at low temperature. *J. Phys. Chem.* **97**, 10761–10768 (1993).
39. Urabe, K., Aika, K.-I. & Ozaki, A. Activation of nitrogen by alkali metal-promoted transition metal. *J. Catal.* **38**, 430–434 (1975).
40. Hikita, T., Kadowaki, Y. & Aika, K.-I. Promoter action of alkali nitrate in Raney ruthenium catalyst for activation of dinitrogen. *J. Phys. Chem.* **95**, 9396–9402 (1991).
41. Hunter, S. M. et al. A study of ¹⁵N/¹⁴N isotopic exchange over cobalt molybdenum nitrides. *ACS Catal.* **3**, 1719–1725 (2013).
42. Rivera Rocabado, D. S. et al. Adsorption states of N₂/H₂ activated on Ru nanoparticles uncovered by modulation-excitation infrared spectroscopy and density functional theory calculations. *ACS Nano* **15**, 20079–20086 (2021).
43. Zimmermann, F. et al. N=N vibrational frequencies and fragmentation patterns of substituted 1-aryl-3,3-dialkyl-triazenes: comparison with other high-nitrogen compounds. *Appl. Spectrosc.* **47**, 986–993 (1993).
44. Rittle, J. & Peters, J. C. An Fe–N₂ complex that generates hydrazine and ammonia via Fe=NNH₂: demonstrating a hybrid distal-to-alternating pathway for N₂ reduction. *J. Am. Chem. Soc.* **138**, 4243–4248 (2016).

Publisher's note Springer Nature remains neutral with regard to jurisdictional claims in published maps and institutional affiliations.

Open Access This article is licensed under a Creative Commons Attribution-NonCommercial-NoDerivatives 4.0 International License, which permits any non-commercial use, sharing, distribution and reproduction in any medium or format, as long as you give appropriate credit to the original author(s) and the source, provide a link to the Creative Commons licence, and indicate if you modified the licensed material. You do not have permission under this licence to share

adapted material derived from this article or parts of it. The images or other third party material in this article are included in the article's Creative Commons licence, unless indicated otherwise in a credit line to the material. If material is not included in the article's Creative Commons licence and your intended use is not permitted by statutory regulation or exceeds the permitted use, you will need to obtain permission directly from the copyright holder. To view a copy of this licence, visit <http://creativecommons.org/licenses/by-nc-nd/4.0/>.

© The Author(s) 2025

Methods

Synthesis of $\text{Ba}_3\text{SiO}_{5-x}\text{H}_y\text{N}_z$

The substitution of oxygen bonded to Si^{4+} with other anions is generally difficult due to the strong Si–O bonding. We have focused on tribarium silicate (Ba_3SiO_5) because its crystal structure is composed of isolated (ortho) SiO_4 tetrahedra and BaO units (isolated O^{2-} coordinated with Ba^{2+} ions) and the substitution of the latter oxygen ions is expected to be much easier than the former. This material is generally synthesized by solid-state reaction at elevated temperatures (over 1,200 °C)^{20,21}. Oxygen substitution with other anions such as H^- and N^{3-} does not readily proceed at low temperatures^{22,23}. $\text{Ba}_3\text{SiO}_{5-x}\text{H}_y\text{N}_z$ powder was prepared by a low-temperature solid-state reaction. Dehydrated SiO_2 (Q-3, Fuji Silysia Chemical) and Ba (99.99%, Aldrich) with a molar ratio of 1:3 were set in a stainless-steel reactor operated in an Ar-filled glovebox. Ammonia gas was introduced to the reactor with a flow rate of 50 ml min⁻¹ at a temperature of approximately –50 °C for 30 min to obtain sufficient liquefied ammonia. Ba was dissolved in the liquefied ammonia under magnetic stirring for another 1 h at the same temperature. The well-sealed reactor was then heated under a temperature programme of 50 °C for 30 min, 75 °C for 30 min and 100 °C for 1 h to obtain a barium amide– SiO_2 ($3\text{Ba}(\text{NH}_2)_2\text{--SiO}_2$) mixture. The mixture was collected in an Ar-filled glovebox after removal of the unreacted ammonia inside the reactor through discharging to the atmosphere by Ar gas introduction at 50 °C. The obtained powder mixture was then wrapped in molybdenum foil and heated in a quartz-tube reactor under a NH_3 flow (100 ml min⁻¹). The heating temperature was increased from room temperature to 400–700 °C with a heating rate of 5 °C min⁻¹ and maintained at the target temperature for 12 h. After cooling to room temperature, the obtained yellow $\text{Ba}_3\text{SiO}_{5-x}\text{H}_y\text{N}_z$ powder was collected and stored in an Ar-filled glovebox for further use. High surface area $\text{Ba}_3\text{SiO}_{5-x}\text{H}_y\text{N}_z\text{--HS}$ powder was prepared by the same method with only the molar ratio of SiO_2 to Ba changed from 1:3 to 1:1.05. The effect of TM impurities such as Fe, Co, Ru and Mo in $\text{Ba}_3\text{SiO}_{5-x}\text{H}_y\text{N}_z$ after the ammonia synthesis test was determined by inductively coupled plasma atomic emission spectroscopy analysis (ICPS-8100, Shimadzu).

Synthesis of Ba_3SiO_5 , $\text{Ba}_3\text{Si}_6\text{O}_9\text{N}_4$ and $\text{BaSi}_2\text{O}_2\text{N}_2$

Ba_3SiO_5 powder was prepared by high-temperature solid-state reaction of well-mixed SiO_2 and BaCO_3 at 1,240 °C in an Ar (95%)/ H_2 (5%) flow. Typically, BaCO_3 (99.95%, High Purity Chemicals) and SiO_2 (Q-3, Fuji Silysia Chemical) in a stoichiometric ratio were thoroughly mixed in a small amount of ethanol and ground in an agate mortar for 1 h. After drying, the mixture was calcined at 1,240 °C in a tube furnace under an Ar (95%)/ H_2 (5%) flow for 12 h. The conventional $\text{Ba}_3\text{Si}_6\text{O}_9\text{N}_4$ and $\text{BaSi}_2\text{O}_2\text{N}_2$ were synthesized by the reported two-step procedures using BaSiO_3 and Ba_2SiO_4 as precursors, respectively^{45,46}. First, a well-mixed BaCO_3 and SiO_2 mixture with a molar ratio of 1:1 (2:1) was calcined in a tube furnace at 1,150 °C for 5 h under a flow of N_2 (95%)/ H_2 (5%) to obtain BaSiO_3 (Ba_2SiO_4). Subsequently, BaSiO_3 (Ba_2SiO_4) and Si_3N_4 with a molar ratio of 3:1 (1:1) were well mixed by grinding and the mixture was further calcined in a tube furnace at 1,350 °C for 5 h under the flow of N_2 (95%)/ H_2 (5%) to obtain $\text{Ba}_3\text{Si}_6\text{O}_9\text{N}_4$ ($\text{BaSi}_2\text{O}_2\text{N}_2$).

Loading of TM nanoparticles

The loading of Ru nanoparticles (NPs) on various supports ($\text{Ba}_3\text{SiO}_{5-x}\text{N}_y\text{H}_z$, Ba_3SiO_5 , $\text{Ba}_3\text{Si}_6\text{O}_9\text{N}_4$, $\text{BaSi}_2\text{O}_2\text{N}_2$, $\text{Ba}(\text{NH}_2)_2$, SiO_2 and MgO) was performed by the chemical vapour deposition method using triruthenium dodecacarbonyl ($\text{Ru}_3(\text{CO})_{12}$, 99%, Aldrich) as a precursor. Typically, a mixture of support powder and $\text{Ru}_3(\text{CO})_{12}$ with the desired weight ratio was set in a well-evacuated silica tube and heated in an oven under the following programme: heating from room temperature to 40 °C (2 °C min⁻¹) for 1 h, heating up to 70 °C (0.25 °C min⁻¹) and holding for 1 h, heating up to 120 °C (0.4 °C min⁻¹) and holding for another 1 h and finally heating up to 250 °C (0.9 °C min⁻¹) and holding for 2 h.

The samples were collected and stored in an Ar-filled glovebox after naturally cooling to the ambient temperature. The actual amount of loaded Ru NPs on the support was determined using an X-ray fluorescence spectrometer (XRF, S8 TIGER, Bruker) (Supplementary Fig. 18). The $\text{Ni}/\text{Ba}_3\text{SiO}_{5-x}\text{N}_y\text{H}_z$ was prepared by heating a mixture of nickelocene and $\text{Ba}_3\text{SiO}_{5-x}\text{N}_y\text{H}_z$ powder at 250 °C for 2 h in a gas flow of N_2 (purity >99.99995%, 2 ml min⁻¹) and H_2 (purity >99.99999%, 6 ml min⁻¹) under a pressure of 0.1 MPa. $\text{Ba}_3\text{SiO}_{5-x}\text{N}_y\text{H}_z$ powder synthesized at 600 °C showed the highest activity when Ru was loaded and thus its structural and catalytic properties were investigated further. The catalytic activities of $\text{Ru}/\text{Ba}(\text{NH}_2)_2$ and Ru/SiO_2 were negligibly low at 300 °C and so are not described in the main text.

Characterization

Powder X-ray diffraction (XRD) patterns of the samples were recorded on a diffractometer (D8 Advance, Bruker) with monochromatic Cu K α radiation ($\lambda = 1.5418$ Å) at a voltage of 40 kV and a current of 40 mA. An X-ray transmitting capsule cell was used to avoid oxidation of the sample during the XRD measurements. The sample purity was determined by Rietveld analysis of the XRD pattern using the TOPAS code (Bruker AXS, version 4.2). Temperature-programmed desorption (TPD) experiments were performed on a catalyst analyser (BELCAT-A, MicrotracBEL). The sample (approximately 50 mg) was heated from room temperature to 950 °C with a heating rate of 10 °C min⁻¹ in a stream of pure He gas (>99.99995%) with a flow rate of 30 ml min⁻¹. The desorbed products during the heating process were monitored using a mass spectrometer (BELMass, MicrotracBEL). Calibration of the N_2 ($m/z = 28$) and H_2 ($m/z = 2$) mass peak areas was conducted by monitoring pulses of $m/z = 28$ and 2 more than five times to obtain average calibration data. The CO-pulse chemisorption experiment was conducted at 50 °C using a He flow (50 ml min⁻¹) and pulses of 0.031 ml (10% CO in He) to evaluate the number of exposed Ru sites by using a catalyst analyser (BELCAT-A, MicrotracBEL). Prior to the experiment, the samples were pretreated with a H_2 (5%)/Ar flow (50 ml min⁻¹) at 400 °C for 60 min, followed by a He flow (50 ml min⁻¹) at 400 °C for 15 min to remove hydrogen atoms adsorbed on the Ru surface. The lattice N^{3-} ions cannot be totally desorbed by the heating treatment. Therefore, the actual amount of lattice N^{3-} ions was further confirmed by an acid dissolution method accompanied by ion chromatography (Supplementary Fig. 45). Solid-state ^1H MAS NMR and ^{29}Si MAS NMR of Ba_3SiO_5 and $\text{Ba}_3\text{SiO}_{5-x}\text{N}_y\text{H}_z$ were performed on a Bruker Biospin DSX-400 spectrometer (Bruker). The Q_0 signal appears at lower magnetic field when O^{2-} ions in the SiO_4 tetrahedral unit are replaced with more electropositive H^- and N^{3-} ions²⁷. Optical diffuse reflectance spectra were measured at room temperature with a spectrophotometer (U-4000, Hitachi) using MgO powder as a background. The Kubelka–Munk transformation was used to convert the measured spectra into absorption spectra. Electron paramagnetic resonance (EPR) measurements of the $\text{Ba}_3\text{SiO}_{5-x}\text{H}_y\text{N}_z$ powder samples were conducted on a spectrometer (E580 X-band, Bruker) (approximately 9.7 GHz) at room temperature. Ru K-edge X-ray absorption fine structure (XAFS) measurements were performed on a synchrotron radiation ring at the NW-10A beamline (Photon Factory, KEK, Japan) using a Si(311) double-crystal monochromator and ionization chambers. A mixture of $\text{Ru}/\text{Ba}_3\text{SiO}_{5-x}\text{H}_y\text{N}_z$ and dehydrated boron nitride powders was pressed into a pellet with a diameter of 10 mm and well-sealed in a polyethylene pack in an Ar-filled glovebox. The collected data were processed using the ATHENA software package. The filtered k^3 -weighted χ spectra were Fourier transformed into r space with a k range 3.0–16.0. High-angle annular dark-field-scanning transmission electron microscopy (HAADF-STEM) observations were conducted using a microscope (ARM-200F, JEOL) operated at 200 kV. The mean particle diameter and distribution of Ru NPs on the support were determined by measuring the size of 200 metal NPs in a STEM image. The specific surface area of the catalysts was determined by the analysis of N_2 adsorption–desorption isotherms collected on a

BELSORP-mini II (MicrotracBEL) at 77 K using the Brunauer–Emmett–Teller (BET) method. X-ray photoelectron spectroscopy (XPS) measurements were performed on a spectrometer (ESCA 3200, Shimadzu) using Mg K α radiation at $<10^{-6}$ Pa. The XPS spectra were calibrated with respect to the C 1s signal at 284.8 eV.

Iodometric titration method

First, 10–20 mg of $\text{Ba}_3\text{SiO}_{5-x}\text{N}_y\text{H}_z$ heated at 650 °C in Ar was set in a glass vial with 1 ml of pure ethanol in an Ar-filled glove box. Then, 2 ml of I_2 solution (5 mmol l^{-1}) and 0.5 ml concentrated hydrochloric acid were added. After magnetic stirring to dissolve the powder, electrons in the sample were consumed by the reduction of I_2 into I^- ions. Then, the residual I_2 was titrated using a standard sodium thiosulfate ($\text{Na}_2\text{S}_2\text{O}_3$) solution (4 mmol l^{-1}). To confirm the endpoint of the titration, a few drops of starch solution were added, which induced a violet colouration. The measurements were repeated three times to obtain an average value.

Ammonia synthesis reactions

Ammonia synthesis over various catalysts (0.1 g) was conducted in a stainless-steel reactor in a gas flow of N_2 (purity $>99.99995\%$, 15 ml min^{-1}) and H_2 (purity $>99.99999\%$, 45 ml min^{-1}) with a pressure of 0.9 MPa and under a steady-state temperature in the range 200–500 °C. The ammonia gas produced was trapped in a 5 mmol l^{-1} sulfuric acid solution to obtain NH_4^{++} solution and the concentration of NH_4^{++} was then monitored using ion chromatography (Prominence, Shimadzu) with a conductivity detector. All the catalysts were treated under the ammonia synthesis conditions at 400 °C for 20 h to remove surface carbon species that remained after the chemical vapour deposition processes for TM loading, as well as to reach a stable catalytic state. The apparent E_a of the measured catalysts was calculated from Arrhenius plots of the ammonia synthesis rates at different temperatures. To avoid the thermal equilibrium effect, the ammonia yield for E_a calculation was less than 20% of that at equilibrium. For comparison with the most active catalyst ($\text{Ba}_2\text{RuH}_6/\text{MgO}$) reported, we also measured the activity under similar experimental conditions (0.03 g catalyst, 1.0 MPa).

Kinetic analysis

The reaction orders of N_2 (α), H_2 (β) and NH_3 (γ) were measured at a steady-state temperature of 340 °C and pressure of 0.9 MPa with a weight hourly space velocity (WHSV) of 36,000 $\text{ml g}^{-1} \text{h}^{-1}$. The activity of the catalysts measured under these conditions was far from the thermal equilibrium to avoid the effects of thermodynamic limits. Calculation of the ammonia synthesis rate (r) was based on equation (1), while equations (2)–(5) were used for the kinetic analysis.

$$r = k \times P_{\text{N}_2}^\alpha \times P_{\text{H}_2}^\beta \times P_{\text{NH}_3}^\gamma \quad (1)$$

$$r = \left(\frac{1}{W}\right) dy_0/d\left(\frac{1}{q}\right) \quad (2)$$

$$\log y_0 = \log\left(\frac{C}{q}\right)^{1/m} \quad (3)$$

$$r = \left(\frac{1}{W}\right)\left(\frac{C}{m}\right)y_0^{(1-m)} \quad (4)$$

$$C = k_2 \times P_{\text{N}_2}^\alpha \times P_{\text{H}_2}^\beta \quad (5)$$

where r , W , y_0 , q and $(1-m)$ represent the NH_3 synthesis rate, the catalyst weight, the outlet NH_3 mole fraction, the total volume flow rate and the reaction order with respect to NH_3 (γ), respectively. k and k_2 are the rate constants. Finally, the α and β parameters can be determined

by plotting the logarithm of a constant within the limited range q (C) versus the partial pressure of N_2 (P_{N_2}) or H_2 (P_{H_2}).

Isotope-labelled experiment and isotopic N_2 exchange measurement

Ammonia syntheses over $\text{Ru}/\text{Ba}_3\text{SiO}_{5-x}\text{N}_y\text{H}_z$ and conventional Ru/MgO from heavy $^{15}\text{N}_2$ (purity 98%) and H_2 were performed in a closed U-shaped glass circulation reactor connected to a gas chromatograph (GC, GC-8A, Shimadzu) with a Chromosorb 103 column and a quadrupole mass spectrometer (M-101QA-TDM, Canon Anelva) using He as the carrier gas. Before the reaction, the catalyst set in the closed glass circulation reactor was evacuated using a vacuum pump with a liquid nitrogen trap to remove the adsorbed water on the catalyst. The mixture of $^{15}\text{N}_2$ (15.0 kPa) and H_2 (45.0 kPa) gases was introduced into the glass reactor and kept circulating using an electromagnetic drive gas circulator. The catalyst (0.1 g) set in the system was heated at 400 °C. The gases produced were abstracted with a gas-sampling loop and flushed out with He gas (0.1 MPa) and then injected into the GC. The outlet gases from the GC were then analysed using the quadrupole mass spectrometer and the corresponding masses of $m/z = 2, 16, 17, 18, 28, 29$ and 30 were monitored as a function of time. The isotope N_2 exchange experiments were conducted using the same system. A mixed gas flow of $^{15}\text{N}_2$ (4 kPa) and $^{14}\text{N}_2$ (16 kPa) was introduced and circulated in the system over the catalyst (0.1 g) heated at 400 °C and the mass signals of $m/z = 28, 29$ and 30 were monitored with respect to the reaction time. The influence of H_2O for this measurement can be ignored because the mass signal of $m/z = 18$ was not increased with reaction time when $^{15}\text{N}_2$ was replaced with $^{14}\text{N}_2$ (Supplementary Fig. 29).

DRIFTS of N_2 absorption experiments

All the samples for DRIFTS of N_2 absorption analysis were pretreated under the ammonia synthesis conditions for 20 h. To confirm the role of V_3 sites in N_2 activation, both $\text{Ba}_3\text{SiO}_{5-x}\text{N}_y\text{H}_z$ and $\text{Ru}/\text{Ba}_3\text{SiO}_{5-x}\text{N}_y\text{H}_z$ catalysts were heated at 650 °C under an Ar atmosphere before the DRIFTS measurements. The powder samples were placed in an alumina sample cup and introduced into a stainless-steel heat chamber equipped with a KBr window (STJ-0123-HP-LTV, S.T. Japan). The samples were heated to above 400 °C in an Ar flow (10 ml min^{-1}) for 5 h to remove surface adsorbed species and were then well evacuated. After the pretreatment, the samples were cooled to -170 °C under vacuum to obtain a background spectrum. The catalysts were then exposed to pure $^{14}\text{N}_2$ (99.99995%) or heavy $^{15}\text{N}_2$ (98%) to collect infrared spectra for adsorbed N_2 . The infrared spectra were measured using a spectrometer (IRTracer-100, Shimadzu) equipped with a mercury–cadmium–tellurium (MCT) detector at a resolution of 4 cm^{-1} .

In situ DRIFTS observations

The powder samples were placed in an alumina sample cup and introduced into a stainless-steel heat chamber equipped with a BaF_2 window (160-1147, S.T. Japan). The samples were placed under a flow of $^{14}\text{N}_2$ (or $^{15}\text{N}_2$) (3 ml min^{-1}) and H_2 (or D_2) (9 ml min^{-1}) at 30 °C for 1 h and the spectra were measured as the background spectra (Supplementary Fig. 37a). Then the sample was gradually heated from 30 to 300 °C and the spectra at different reaction temperatures were recorded on a spectrometer (FT/IR-6XV, JASCO) equipped with a mercury–cadmium–tellurium (MCT) detector at a resolution of 0.25 cm^{-1} . Figure 4c shows the difference spectra using the spectra measured at 30 °C under the same reaction gas atmosphere as the background spectra (Supplementary Fig. 37a). The band at 1,424 cm^{-1} due to the $\nu(^{15}\text{N}=^{14}\text{N})$ is also observed, which may be caused by the recombination of lattice ^{14}N and ^{15}N in $\text{Ba}_3\text{SiO}_{5-x}\text{N}_y\text{H}_z$ at the elevated temperature.

DFT calculations

All structure relaxation and electronic structure calculations were performed using the DFT method as implemented in the Vienna ab

initio simulation package (VASP)⁴⁷. The calculation settings of 600 eV cutoff energy and Γ -centred k -points with a mesh resolution of $2 \times 0.04 \text{ \AA}$ were adopted for all structures. To obtain the total energy, the possible structures were fully relaxed using the Perdew–Burke–Ernzerhof (PBE) functional with the projector augmented wave (PAW) method until the convergence criteria of energy and force were met (less than $1.0 \times 10^{-6} \text{ eV}$ and $1.0 \times 10^{-2} \text{ eV \AA}^{-1}$, respectively)⁴⁸. On the basis of the chemical stoichiometry determined by the experiments, the computational models $\text{Ba}_3\text{SiO}_{5-2x}\text{N}_x\text{H}_x$ (N–H pair replaces O–O pair), $\text{Ba}_3\text{SiO}_{5-y}\text{H}_{2y}$ (H–H pair replaces oxygen) and $\text{Ba}_3\text{SiO}_{5-2x-y}\text{N}_x\text{H}_{x+2y}$ (N–H pair replaces O–O pair with an extra H–H pair) were derived from the optimized Ba_3SiO_5 primitive cell. As for the H–H pair, two hydrogen atoms were placed at one oxygen site with the H–H distance set to approximately 0.8 \AA for charge compensation. Among all the computation models listed in Supplementary Tables 2–4, the computation model of $\text{Ba}_3\text{SiO}_{5-2x-y}\text{N}_x\text{H}_{x+2y}$ with $x = 1$ and $y = 0.5$ (that is $\text{Ba}_3\text{SiO}_{2.5}\text{NH}_2$) well reproduces the experimental result (Supplementary Table 1) and therefore, it was selected as a benchmarking computational model for further reaction pathway calculations. The density of states of the $\text{Ba}_3\text{SiO}_{2.5}\text{NH}_2$ system was calculated using the tetrahedron method with a Γ -centred k -point mesh of $7 \times 7 \times 4$. The atom-projected densities of states were evaluated with Wigner–Seitz radii (R_{WS}) of 1.62 \AA satisfying $R_{\text{WS}} = (3V_{\text{cell}}/4\pi N)^{1/3}$, where V_{cell} is the unit cell volume (682.89 \AA^3) and N is the number of total atoms in the unit cell ($N = 38$). The calculation settings of 400 eV cutoff energy and a Monkhorst–Pack mesh k -point grid of $2 \times 2 \times 1$ were adopted for surface structures. The bottom two layers were fixed for the slab model. The $\text{Ba}_3\text{SiO}_2\text{NH}_2(001)$ surface is the most stable among the low-index surfaces calculated using the DFT method. At the (001) surface, SiO_2NH units are preferentially exposed over Ba_6H_2 units. Therefore, the anion vacancy site is formed at SiO_2NH units on the $\text{Ba}_3\text{SiO}_2\text{NH}_2(001)$ surface in our simulation. The convergence criteria were set as $1.0 \times 10^{-5} \text{ eV}$ in energy and $<1.0 \times 10^{-2} \text{ eV \AA}^{-1}$ in force for the structure relation ($1.0 \times 10^{-5} \text{ eV}$ in energy and $<5.0 \times 10^{-2} \text{ eV \AA}^{-1}$ in force for intermediates and transition state structures in the climbing image nudged elastic band method^{49,50}, reaction path analysis). These calculation conditions are almost the same as those in the previously reported work for the simulation of catalytic ammonia synthesis⁵¹.

Data availability

All data supporting the findings of this study are available within this Article and its Supplementary Information. Source data are provided with this paper.

References

- Luong, V. D. & Lee, H.-R. Synthesis and luminescence properties of $\text{Sr}/\text{SmSi}_5\text{N}_8:\text{Eu}^{2+}$ phosphor for white light-emitting-diode. *J. Korean Inst. Surf. Eng.* **47**, 192–197 (2014).
- Yuan, B.-G. et al. Preparation and luminescence properties of single-phase $\text{BaSi}_2\text{O}_7\text{N}_2:\text{Eu}^{2+}$, a bluish-green phosphor for white light-emitting diodes. *J. Electrochem. Soc.* **157**, J364 (2010).
- Kresse, G. & Furthmüller, J. Efficient iterative schemes for ab initio total-energy calculations using a plane-wave basis set. *Phys. Rev. B* **54**, 11169–11186 (1996).
- Blöchl, P. E. Projector augmented-wave method. *Phys. Rev. B* **50**, 17953–17979 (1994).
- Henkelman, G. & Jónsson, H. A climbing image nudged elastic band method for finding saddle points and minimum energy paths. *J. Chem. Phys.* **113**, 9901–9904 (2000).
- Henkelman, G. & Jónsson, H. Improved tangent estimate in the nudged elastic band method for finding minimum energy paths and saddle points. *J. Chem. Phys.* **113**, 9978–9985 (2000).
- Nako, T., Tada, T. & Hosono, H. Transition metal-doped Ru nanoparticles loaded on metal hydrides for efficient ammonia synthesis from first principles. *J. Phys. Chem. C* **124**, 1529–1534 (2020).

Acknowledgements

We thank S. Kitani for assistance with the solid-state NMR measurements. This study was supported by the FOREST Program (No. JPMJFR203A) from the Japan Science and Technology Agency (JST) and Kakenhi Grants-in-Aid (No. JP22H00272, JP24H02203, JPH02204) from the JSPS. Part of this work was supported by the JST-Mirai Program (JPMJMI21E9) from JST, a project (JPNP21012) commissioned by the New Energy and Industrial Technology Development Organization (NEDO) and a project in collaboration with Tsubame BHB. Z.Z. was supported by a JSPS fellowship for International Research Fellows (No. JP21F21032). The XAFS experiments were conducted with the help of H. Abe and Y. Niwa under the approval of the Photon Factory Program Advisory Committee (PF-PAC, No. 2021G543). We thank the Materials Analysis Division, Open Facility Center, Tokyo Institute of Technology, for conducting the inductively coupled plasma atomic emission spectroscopy analysis.

Author contributions

M.K. and H.H. conceived and supervised the project. Z.Z., M.K. and H.H. wrote the paper with contributions from all co-authors. Z.Z. performed the synthesis, characterization and catalytic measurements with the assistance of J.K. and K.O., Y.J., J.L. and Z.Z. performed the EPR measurements and analysis. M.S. performed the STEM measurements. Z.Z. and Y.J. performed the XPS, isotope-labelled and DRIFTS of the N_2 absorption experiments. M.M. performed the XAFS measurements. T.W., S.M., K.M. and T.T. simulated the crystal structures and reaction pathways.

Competing interests

The authors declare no competing interests.

Additional information

Supplementary information The online version contains supplementary material available at <https://doi.org/10.1038/s41557-025-01737-8>.

Correspondence and requests for materials should be addressed to Tomofumi Tada, Hideo Hosono or Masaaki Kitano.

Peer review information *Nature Chemistry* thanks Angela Daisley and the other, anonymous, reviewer(s) for their contribution to the peer review of this work.

Reprints and permissions information is available at www.nature.com/reprints.